Acoustic dipole radiation model for magnetoacoustic tomography with magnetic induction*

Li Yi-Ling(李宜令)[a], Ma Qing-Yu(马青玉)[b)†],
Zhang Dong(章 东)[c], and Xia Rong-Min(夏荣民)[d]

[a] *Department of Educational Technology, Nanjing Normal University, Nanjing* 210097, *China*
[b] *Key Laboratory of Optoelectronics of Jiangsu Province, School of Physics and Technology, Nanjing Normal University, Nanjing* 210046, *China*
[c] *Institute of Acoustics, Nanjing University, Nanjing* 210093, *China*
[d] *University of Arkansas for Medical Science, Little Rock, AR* 72205, *USA*

(Received 22 January 2011; revised manuscript received 18 March 2011)

An acoustic dipole radiation model for magnetoacoustic tomography with magnetic induction (MAT-MI) is proposed, based on the analyses of one-dimensional tissue vibration, three-dimensional acoustic dipole radiation and acoustic waveform detection with a planar piston transducer. The collected waveforms provide information about the conductivity boundaries in various vibration intensities and phases due to the acoustic dipole radiation pattern. Combined with the simplified back projection algorithm, the conductivity configuration of the measured layer in terms of shape and size can be reconstructed with obvious border stripes. The numerical simulation is performed for a two-layer cylindrical phantom model and it is also verified by the experimental results of MAT-MI for a tissue-like sample phantom. The proposed model suggests a potential application of conductivity differentiation and provides a universal basis for the further study of conductivity reconstruction for MAT-MI.

Keywords: magnetoacoustic tomography with magnetic induction, acoustic dipole radiation, beam pattern, biological tissues

PACS: 43.80.Ev, 72.55.+s, 73.50.Rb **DOI:** 10.1088/1674-1056/20/8/084302

1. Introduction

In the past decades, several non-invasive imaging techniques, such as electrical impedance tomography (EIT),[1−3] magnetic induction tomography (MIT)[4,5] and magnetic resonance electrical impedance tomography (MREIT),[6−8] have been proposed to image the electrical impedance distribution of biological tissues with improved image contrast with the help of a broad range of impedance value. However, the EIT technique is limited by the shielding effect[9] of insulating tissues for current injection. The ultimate spatial resolution of EIT or MIT needs further improvement in order to achieve the high resolution required for electrical impedance imaging, and the practical application of MREIT is limited by the high-level current injection, low-level signal-to-noise ratio and high cost. A novel imaging modality of magnetoacoustic tomography with magnetic induction (MAT-MI)[10−19] was recently proposed to improve spatial resolution and image contrast without current injection.

Compared with other imaging modalities, MAT-MI has shown improved reliability without physical contact and the shielding effect for magnetic excitation and acoustic propagation.[11−14] Xu and He[11] demonstrated the feasibility of the MAT-MI approach for electrical impedance imaging. Xia *et al.*[14] performed a three-dimensional (3D) image reconstruction with multi-layer measurement for a cylindrical phantom model. Li *et al.*,[16] and Ma and He[17,18] proposed a theoretical study for MAT-MI using the acoustic straight line propagation mode with a focused transducer and neglecting acoustic diffraction. A two-dimensional (2D) inverse problem of conductivity reconstruction was also investigated by using the finite element method (FEM)[19] to evaluate the performance of MAT-MI.

In previous studies of MAT-MI, each Lorentz-force-induced tissue vibration was considered to be

*Project supported by the National Basic Research Program of China (Grant No. 2011CB707900), the National Natural Science Foundation of China (Grant No. 10974098), the Natural Science Foundation of Jiangsu Province, China (Grant No. BK2009407), and the Specialized Research Fund for Doctoral Program of High Education of China (Grant No. 20093207120003).

†Corresponding author. E-mail: maqingyu@njnu.edu.cn

© 2011 Chinese Physical Society and IOP Publishing Ltd

a point acoustic source to produce spherical acoustic propagation based on Green's theorem. However, the Lorentz-force-induced 1D tissue vibration in MAT-MI is along the normal direction of eddy current and the bi-directional vibration produces acoustic waves with opposite vibration phases, which should be considered as an acoustic dipole to generate 3D acoustic propagation with corresponding radiation pattern.[20]

In the present study, an acoustic dipole radiation model is proposed to solve the forward problem of MAT-MI for a planar piston transducer, based on the analysis of 1D magnetic induction, 1D acoustic vibration, 3D acoustic dipole radiation, acoustic pressure integration and transducer waveform detection. The analytical solutions of MAT-MI are deduced in explicit formulae to describe the acoustic propagation, the acoustic pressure superposition and transducer waveform collection. To validate the proposed theory, numerical simulations of acoustic dipole radiation, acoustic waveform collection and 2D magnetoacoustic tomographic image reconstruction for a cylindrical phantom model with several geometric specifications are conducted. Based on the radiation pattern analysis for each acoustic dipole, the reason why the transducer-collected waveforms can provide only the acoustic signal at the conductivity boundary is clearly explained. It is also demonstrated that the configurations of the scanned layer in terms of shape and size can be reconstructed without inner conductivity distribution visualization. The experimental paradigms[18] for a two-layer cylindrical tissue-like sample phantom show good agreement with the numerical simulation results. The favourable results suggest the potential application of MAT-MI to electrical impedance imaging and provides a universal basis for the further study of conductivity reconstruction.

2. Theory and method

In the MAT-MI system shown in Fig. 1, a conductive object is placed in a static magnetic field $\boldsymbol{B}_0 = B_0\hat{z}$ (the bold variable refers to a vector and the hatted variable denotes the unit vector in this paper) and a time-varying pulsed magnetic field $\boldsymbol{B} = B(t)\hat{z}$ generated by a magnet and a stimulating coil, respectively. The coil is excited by an electric current pulse to generate a pulsed magnetic field, which can induce eddy currents inside the conductive object volume. For simplicity, both the static and the pulsed magnetic fields are considered to be homogeneous in the region covering the entire object volume V, while the secondary magnetic field generated by the eddy current is neglected for the low conductivity of tissues. Due to the interaction between the static magnetic field and the induced eddy current, an acoustic wave can be generated by the Lorentz-force-induced acoustic vibration within the object. The generated acoustic pressure p satisfies the wave equation[21,22]

$$\nabla^2 p - \frac{1}{c^2}\frac{\partial^2 p}{\partial t^2} = -\nabla \cdot [\boldsymbol{J}(\boldsymbol{r}) \times \boldsymbol{B}_0], \qquad (1)$$

where the acoustic source strength is a given function of $Q(\boldsymbol{r}) = \nabla \cdot [\boldsymbol{J}(\boldsymbol{r}) \times \boldsymbol{B}_0]$ at the point $\boldsymbol{r}(x, y, z)$ inside the object, ∇ is the divergence operator, ∇^2 is the Laplacian operator, and c is the acoustic velocity. The acoustic waveforms can be detected by the transducers placed at $\boldsymbol{r}'(x', y', z')$ around the object for the acoustic diffraction transmission in a 3D free space.

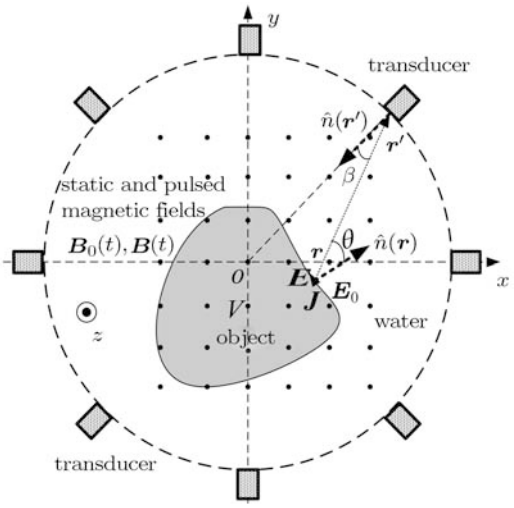


Fig. 1. Illustration of the MAT-MI system.

For the magnetic induction in the MAT-MI system with a low frequency of 0.5 MHz, the eddy and the displacement currents are too small to disturb the source magnetic field significantly. For biological tissues, the displacement current is negligible against the induced conduction current.[12] Supposing that an object with a uniform conductivity σ is immersed in an insulating medium of $\sigma_0 = 0$ S/m, the induced electrical intensity $\boldsymbol{E}$ in the object is governed by Faraday's law as $\nabla \times \boldsymbol{E} = -\partial \boldsymbol{B}(t)/\partial t$ and the induced eddy current density can be described as $\boldsymbol{J}(\boldsymbol{r}) = \sigma \boldsymbol{E}(\boldsymbol{r})$ based on Ohm's law. The induced electrical field also satisfies the boundary condition $\hat{n} \times (\boldsymbol{E} - \boldsymbol{E}_0) = 0$ at the conductive-insulator junction, where $\boldsymbol{E}_0$ is the electrical intensity in the insulating medium and $\hat{n}$ is the unit normal to $\boldsymbol{E}_0$. Supposing that the pulsed magnetic field is a step function $\varepsilon(t)\hat{z}$ in MAT-MI system, then $\nabla \times \boldsymbol{E}_\delta(\boldsymbol{r}) = -\delta(t)\hat{z}$ and

the induced eddy current density $\boldsymbol{J}_\delta(\boldsymbol{r})\delta(t)$ are perpendicular to the external pulsed magnetic field. The induced Lorentz force density $\boldsymbol{F}_\mathrm{L} = [\boldsymbol{J}_\delta(\boldsymbol{r})\delta(t) \times \boldsymbol{B}_0]$ is along the normal direction of the induced eddy current in the xy plane, so the corresponding acoustic source strength $Q_\delta(\boldsymbol{r}) = \boldsymbol{\nabla} \cdot [\boldsymbol{J}_\delta(\boldsymbol{r})\delta(t) \times \boldsymbol{B}_0]$ at point $\boldsymbol{r}$ produces 1D tissue vibration along the direction of the Lorentz force. For a conductivity homogenous medium, the induced eddy current lines are closed loops and the eddy current increases with the dimension for $\oint [\boldsymbol{J}_\delta(\boldsymbol{r})/\sigma]\,\mathrm{d}L = -\iint \delta(t)\mathrm{d}S$, where L and S are the corresponding perimeter and area, respectively. It reaches a maximum at the conductive boundary with a shape similar to the cross-sectional geometry of the medium. Due to the differential effect, the acoustic source strength inside a low conductivity medium is much smaller than that generated at the conductivity boundary. Based on Green's theorem for a monopole acoustic point source, the acoustic pressure transmitted from the source position $\boldsymbol{r}$ to the receiver position $\boldsymbol{r}'$ can be written as $Q_\delta(\boldsymbol{r}) \exp[\mathrm{j}(\omega t - k|\boldsymbol{r}' - \boldsymbol{r}|)] / [4\pi|\boldsymbol{r}' - \boldsymbol{r}|]$,[20−22] where ω and k are the angular frequency and the wave number of the acoustic signal, respectively.

In the microscopic sketch map of acoustic dipole radiation in MAT-MI, as shown in Fig. 2, the direction of the Lorentz force at position $\boldsymbol{r}$ is along the normal direction of the induced eddy current. The media compression at the right side $\boldsymbol{r}_+$ and decompression at the left side $\boldsymbol{r}_-$ produce two acoustic vibration sources with opposite phases and each one can produce acoustic transmission in 3D space. Unlike monopolar acoustic point source radiation, the two acoustic point sources with opposite phases should be pictured as the two monopole sources of a dipole vector and the acoustic dipole radiation should be considered in 3D diffraction transmission mode. Taking pressure superposition as the two monopole sources, the dipole produced acoustic pressure transmitted from $\boldsymbol{r}$ to $\boldsymbol{r}'$ can be expressed as[20−22]

$$p(\boldsymbol{r}', \boldsymbol{r}) = \frac{Q_\delta(\boldsymbol{r}_+)}{4\pi r_+} \exp[\mathrm{j}(\omega t - k\boldsymbol{r}_+)] - \frac{Q_\delta(\boldsymbol{r}_-)}{4\pi r_-} \exp[\mathrm{j}(\omega t - kr_-)], \qquad (2)$$

where $r_+ = |\boldsymbol{r}' - \boldsymbol{r}_+|$ and $r_- = |\boldsymbol{r}' - \boldsymbol{r}_-|$. Supposing that the distance l between the two point sources of the dipole is much smaller than the transmission distance $|\boldsymbol{r}' - \boldsymbol{r}|$ and it is also small enough compared with the acoustic wavelength, the acoustic transmission distances can be approximated to $r_+ \approx r + l\cos\theta/2$ and $r_- \approx r - l\cos\theta/2$ respectively, where θ is the angle between the normal direction of $\hat{n}(\boldsymbol{r})$ and the transmission path $\boldsymbol{r}' - \boldsymbol{r}$ (see Fig. 2). When the frequency is not too high for $kl < 1$, $Q_\delta(\boldsymbol{r}) \approx Q_\delta(\boldsymbol{r}_+) \approx Q_\delta(\boldsymbol{r}_-)$ and $r \approx r_+ \approx r_-$. Considering the opposite vibration phases, the dipole-produced acoustic pressure $p(\boldsymbol{r}', \boldsymbol{r})$ transmitted from $\boldsymbol{r}$ to $\boldsymbol{r}'$ can be simplified into[20−22]

$$p(\boldsymbol{r}', \boldsymbol{r}) = \eta \frac{\boldsymbol{\nabla} \cdot [\boldsymbol{J}_\delta(\boldsymbol{r})\delta(t) \times \boldsymbol{B}_0]}{4\pi|\boldsymbol{r}' - \boldsymbol{r}|} \cos\theta, \qquad (3)$$

where $\eta = -\mathrm{j}\,kl$ is the dimensionless constant for a specific system and the transmission time is set to be $t = |\boldsymbol{r}' - \boldsymbol{r}|/c$ to satisfy $\exp[\mathrm{j}(\omega t - k|\boldsymbol{r}' - \boldsymbol{r}|)] = 1$. It is clearly indicated that the radiation of the acoustic dipole of MAT-MI is inversely proportional to the transmission distance $|\boldsymbol{r}' - \boldsymbol{r}|$ with a radiation pattern of $\cos\theta$.

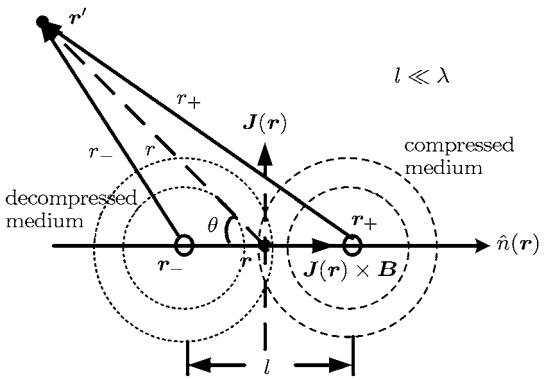


Fig. 2. Sketch map of acoustic dipole radiation in MAT-MI.

As shown in Fig. 1, a planar circular piston transducer with the surface radius a is located around the object to detect the propagated acoustic pressures with the transducer pointing to the origin. The acoustic signals transmitted from the vibration sources inside the object produce a pressure superposition on the transducer surface. If there is an angle β between the unit normal $\hat{n}(\boldsymbol{r}')$ of the transducer surface and the transmission path $|\boldsymbol{r}' - \boldsymbol{r}|$, the beam pattern $|2\mathrm{J}_1(ka\sin\beta)/(ka\sin\beta)|$ of the planar transducer should be considered[20,22] and the transducer-detected pressure $p_\mathrm{R}(\boldsymbol{r}', \boldsymbol{r})$ transmitted from the acoustic dipole source position $\boldsymbol{r}$ to $\boldsymbol{r}'$ can be written as

$$p_\mathrm{R}(\boldsymbol{r}', \boldsymbol{r}) = \xi\eta \frac{\boldsymbol{\nabla} \cdot [\boldsymbol{J}_\delta(\boldsymbol{r})\delta(t) \times \boldsymbol{B}_0]}{4\pi|\boldsymbol{r}' - \boldsymbol{r}|} \times \left|\frac{2\mathrm{J}_1(ka\sin\beta)}{ka\sin\beta}\right| \cos\theta, \qquad (4)$$

where ξ is the acoustic pressure conversion efficiency of the transducer and $\mathrm{J}_1(ka\sin\beta)$ is the regular cylindrical Bessel function of first order.

By extending the dipole source position $\boldsymbol{r}$ to the entire object volume V and considering the time delay of the transmission distance, the acoustic pressure detected by the planar transducer at $\boldsymbol{r}'$ can be described as the volume integral over $p_{\mathrm{R}}(\boldsymbol{r}', \boldsymbol{r})$

$$p_{\mathrm{R}}(\boldsymbol{r}', t) = \xi\eta \iiint_V \frac{\boldsymbol{\nabla}\cdot[\boldsymbol{J}_\delta(\boldsymbol{r})\times\boldsymbol{B}_0]}{4\pi|\boldsymbol{r}'-\boldsymbol{r}|}\left|\frac{2\mathrm{J}_1(ka\sin\beta)}{ka\sin\beta}\right| \times\cos\theta\mathrm{d}\boldsymbol{r}\otimes\delta\left(t-\frac{|\boldsymbol{r}'-\boldsymbol{r}|}{c}\right), \quad (5)$$

where $\otimes$ is the convolution operator and $\delta(t-|\boldsymbol{r}'-\boldsymbol{r}|/c)$ introduces the time delay of the acoustic transmission distance $|\boldsymbol{r}'-\boldsymbol{r}|$.

However, for current excitation of a stimulating coil, the pulsed magnetic signal of a step function is impossible to be generated. So the waveform of the pulsed magnetic field $\boldsymbol{B}(t)$ should be considered as $B(t)\hat{z} = [\partial B(t)/\partial t]\otimes\varepsilon(t)\hat{z}$, where the pulsed magnetic field of a step function $\varepsilon(t)\hat{z}$ is used for $p_{\mathrm{R}}(\boldsymbol{r}', t)$ derivation. Meanwhile, each transducer has its own impulse response $S(t)$ to produce a time-series vibration for the acoustic excitation of a delta function. Combining the waveforms of $B(t)$ and $S(t)$, the transducer-collected acoustic waveform at $\boldsymbol{r}'$ can be described as

$$w_{\mathrm{R}}(\boldsymbol{r}', t) = \xi\eta \iiint_V \frac{\boldsymbol{\nabla}\cdot[\boldsymbol{J}_\delta(\boldsymbol{r})\times\boldsymbol{B}_0]}{4\pi|\boldsymbol{r}'-\boldsymbol{r}|}\left|\frac{2\mathrm{J}_1(ka\sin\beta)}{ka\sin\beta}\right| \times\cos\theta\mathrm{d}\boldsymbol{r}\otimes\delta\left(t-\frac{|\boldsymbol{r}'-\boldsymbol{r}|}{c}\right) \otimes S(t)\otimes\frac{\partial B(t)}{\partial t}. \quad (6)$$

Therefore, each transducer-collected acoustic waveform at position $\boldsymbol{r}'$ can be expressed as the convolution result of the system transfer function $h(t)$ and the acoustic pressure $p_{\mathrm{R}}(\boldsymbol{r}', t)$. Here, the system transfer function $h(t) = S(t)\otimes[\partial B(t)/\partial t]$ is produced by the impulse response of the transducer and the waveform of the pulsed magnetic field of the MAT-MI system. $p_{\mathrm{R}}(\boldsymbol{r}', t)$ can be defined as the conductive transfer function that is determined only by the conductivity distribution of the conductive object.

In the image reconstruction process, the acoustic source cannot be identified accurately from each waveform. However, it can be achieved using the tomographic technique for the waveform $w_{\mathrm{R}}(\boldsymbol{r}', t)$ collected around the object. In the MAT-MI system, the waveforms of the received acoustic signals are used to reconstruct the image by the means of a simplified back projection algorithm for diffraction acoustic sources[11,23−25]

$$I(\boldsymbol{r}) = \frac{1}{2\pi c^2}\int_0^{2\pi}\frac{\boldsymbol{n}(\boldsymbol{r}')(\boldsymbol{r}'-\boldsymbol{r})}{|\boldsymbol{r}'-\boldsymbol{r}|^2}w_{\mathrm{R}}(\boldsymbol{r}', t)\mathrm{d}\varphi, \quad (7)$$

where $I(\boldsymbol{r})$ is the reconstructed intensity at $\boldsymbol{r}$ inside the measured scope and φ is the measured angle of the transducer. The transmission distance can be calculated with the time delay from each time-series waveform collected around the object as $|\boldsymbol{r}'-\boldsymbol{r}| = ct$.

3. Numerical simulations and experimental results

To verify the validity of the proposed theory for the forward problem of MAT-MI, 3D simulations were conducted for a two-layer eccentric cylindrical phantom model with a height of 72 mm, as shown in Fig. 3(a) and the corresponding cross section is presented in Fig. 3(b) with the conductivity value displayed in different gray scales. The conductivities of the outer and the inner media were set as $\sigma_1 = 1$ S/m (simulating parenchyma) and $\sigma_2 = 0$ S/m (simulating fat) respectively. The diameters of the outer and inner media were set to be 72 mm and 36 mm centred at the origin and (6, −6) mm, respectively. The transducer scans around the object in a circular orbit with a radius of 60 mm.

To simplify the numerical calculation, the entire object was immersed into distilled water of $\sigma_0 \approx 0$ S/m for acoustic coupling, and the acoustic system was considered to be acoustically homogeneous without acoustic reflection, dispersion and attenuation consideration.[25] The acoustic velocities in the media were both set to be 1500 m/s. The sampling rate of the acoustic waveform collection and the corresponding calculation grid were set to be 5 MHz and 0.3 mm, respectively. The central frequency of the transducer and the frequency of the pulsed magnetic field were both set to be 0.5 MHz. The waveform of the magnetic signal and the impulse response were simulated as a semi-cycle cosine wave and a three-cycle damping cosine pulse, respectively. The planar transducer was placed in the central layer of the object at $z = 0$ mm and the radius of the transducer surface was optimized to be 0.1 mm to lower the influence of transducer aperture.

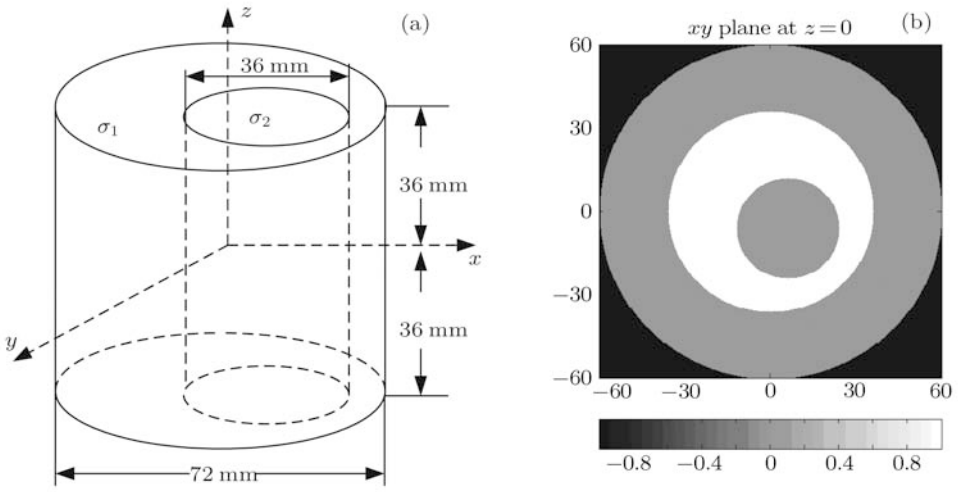


Fig. 3. (a) 3D configuration of the two-layer cylindrical model and (b) 2D conductivity distribution of the cross section. (in mm).

In the simulations, the transducer-collected acoustic waveforms at the angles from 0° to 359° were calculated based on Eq. (6) with a step angle of 1°. The following calculation flowchart was employed for each measured angle:

(i) calculate the coordinate $\boldsymbol{r}'$ for the transducer at the measured angle;

(ii) calculate the acoustic source strength $Q(\boldsymbol{r})$ within the object;

(iii) calculate the acoustic pressure $p(\boldsymbol{r}', \boldsymbol{r})$ transmitted from $\boldsymbol{r}$ to $\boldsymbol{r}'$ based on the acoustic dipole radiation theory;

(iv) integrate the acoustic pressure $p(\boldsymbol{r}', \boldsymbol{r})$ over the entire object (240 layers from −36 mm to 36 mm) to obtain the conductive transfer function $p_{\mathrm{R}}(\boldsymbol{r}', t)$;

(v) simulate the transducer-collected acoustic waveform $w_{\mathrm{R}}(\boldsymbol{r}', t)$ using the convolution operation between the conductive transfer function $p_{\mathrm{R}}(\boldsymbol{r}', t)$ and the system transfer function $h(t)$.

Figure 4(a) shows the normalized pressure of $p_{\mathrm{R}}(\boldsymbol{r}', t)$ obtained at an angle of 100° and figure 4(b) displays the corresponding normalized acoustic waveform $w_{\mathrm{R}}(\boldsymbol{r}', t)$ for comparison. Four pressure jumps are clearly observed at about 16, 25, 49 and 64 μs in Fig. 4(a), representing the peak pressure values generated at the conductivity boundaries with the normal direction of the induced eddy current $\boldsymbol{J}(\boldsymbol{r})$ perpendicular to the transducer surface as $\hat{n}(\boldsymbol{r}') = \hat{n}(\boldsymbol{r})$. The inverse acoustic pressures describe the opposite vibration phases induced by the opposite conductivity change directions along the transmission path. For example, the positive pressure at 16 μs represents the positive conductivity change from 0 S/m to 1 S/m, while the negative pressure at 64 μs is for the negative conductivity change from 1 S/m to 0 S/m of the outer medium. The pressure amplitude of each medium is asymmetric due to the differences in transmission distance and angle of each acoustic dipole radiation from $\boldsymbol{r}$ to $\boldsymbol{r}'$, even though the configurations of the outer and inner media are symmetric circles. So there is continuous acoustic pressure damping between the jumps from the maximal to the minimal values and the amplitude difference comes from the integral over all the acoustic dipole sources in the object volume.

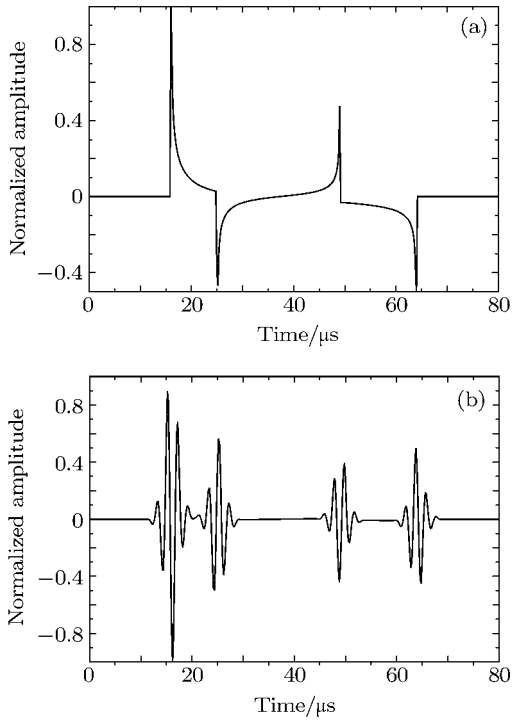


Fig. 4. (a) Normalized acoustic pressure $p_{\mathrm{R}}(\boldsymbol{r}', t)$ measured at an angle of 100° and (b) corresponding detected waveform $w_{\mathrm{R}}(\boldsymbol{r}', t)$.

Due to the vibration of the impulse response of

the transducer in the convolution operation with the acoustic pressure $p_{\mathrm{R}}(\boldsymbol{r}', t)$, four obvious wave clusters are generated in the collected waveform $w_{\mathrm{R}}(\boldsymbol{r}', t)$ as shown in Fig. 4(b), which are produced by the four jumps of $p_{\mathrm{R}}(\boldsymbol{r}', t)$. The different amplitudes and phases of the wave clusters represent the differences in intensity and polarity of the acoustic pressure in $p_{\mathrm{R}}(\boldsymbol{r}', t)$ respectively. Meanwhile, the wave clusters produced by the continuous waves (for example, from 25 μs to 49 μs) are almost eliminated after the convolution operation.

Based on the back projection algorithm of Eq. (7), the acoustic tomographic image of MAT-MI was reconstructed as illustrated in Fig. 5(a) with 360 simulated waveforms. The configurations in terms of shapes and sizes of the outer and inner media of the object are clearly displayed, while the conductivity distribution inside each conductive homogenous medium cannot be visualized. In addition, an obvious stripe at each conductive

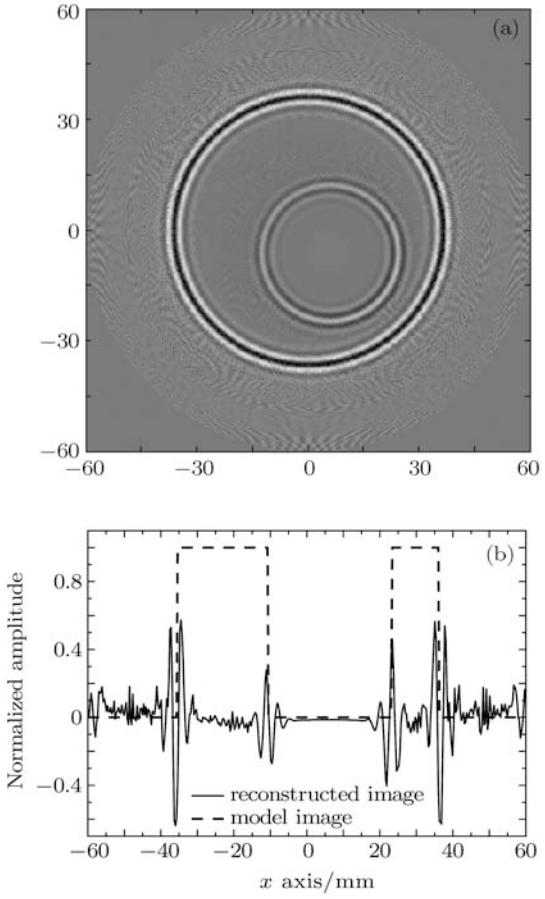


Fig. 5. (a) Reconstructed image using the detected waveforms and (b) its 1D distribution (solid line) at $y = 0$ mm with the corresponding conductivity distribution of the model for comparison (dashed line).

boundary makes a wide borderline between the adjacent media, which is introduced by the impulse response of the receiver. The boundary brightness of the outer medium is higher than that of the inner medium because of the higher induced eddy current. As shown in Fig. 5(b), the 1D distribution (solid line) of the reconstructed image at $y = 0$ mm identifies the accurate positions of the conductivity boundaries, which accords well with the corresponding conductivity distribution (dashed line) of the model. In addition, the opposite vibration phases at -36 mm and -10 mm represent the inverse conductivity changes, and their amplitudes also indicate the Lorentz force difference at the conductivity boundaries of the outer and inner media.

Although the simulations had verified the validation of the proposed theory for the forward problem of MAT-MI, it would be more desirable to test its effectivity further with the experimental data. The acoustic waveforms were extracted from the measured data,[18] and then the image was reconstructed based on Eqs. (6) and (7). In the experiment, a planar piston transducer (V301, 0.5 MHz, Panametrics) was used as the receiver. The phantom model used in the experiment was a two-layer cylindrical sample with 0% saline gel (0 S/m, about 30-mm diameter) used as the inner medium and 0.5% saline gel (0.95 S/m, about 50-mm diameter) serving as the outer medium. The experimental results of the acoustic waveform and the reconstructed image accord well with the theoretical predictions. As shown in Fig. 6(a), the collected acoustic waveform at an angle of 270° displays four clusters with corresponding positions, amplitudes, and vibration phases, which represent the four conductivity boundaries of the model. It is clear that the wave clusters of the outer (26 μs and 59 μs) or inner (32 μs and 49 μs) medium are in opposite vibration phases and the amplitude at 59 μs is even higher than that at 26 μs. It is consistent with the theoretical prediction of the acoustic dipole radiation model and further proves that the acoustic pressure is determined by not only the transmission distance but also the transmission angle. However, the high level noise introduced by the experimental system is also obviously revealed in the waveform.

The reconstructed image in Fig. 6(b) presents the conductivity configuration of the cross section of the cylindrical phantom. The stripes at the conductivity boundaries with the opposite vibration phases and corresponding amplitudes are displayed in different brightnesses. However, some boundaries are blurred because of the acoustic pressure superposition in the

experiment, including the conductivity abnormity of the phantom, pressure counteraction on the large-scale transducer surface and the finite sampling number, low level SNR, and so on.

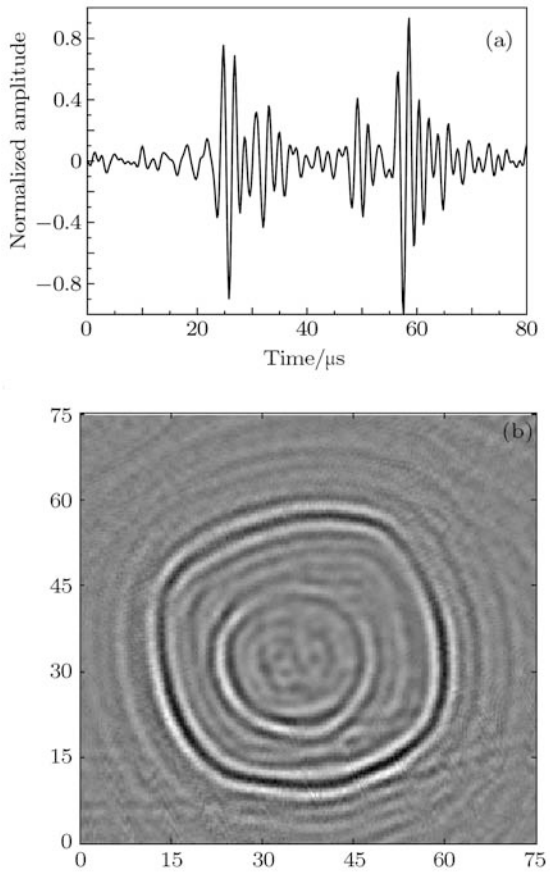


Fig. 6. (a) Experimental acoustic waveform detected at an angle of 270°, and (b) reconstructed image (in mm).

4. Discussion

In thermoacoustic tomography (TAT) with microwave radiation, thermally induced tissue vibration is a pulsating spherical source with an omnidirectional radiation pattern and the acoustic pressure can be calculated using the Green's function. For the point acoustic radiation assumption, the collected wave clusters are in the same vibration phase and the higher amplitude can be achieved for closer transmission because the acoustic pressure is only inversely proportional to the transmission distance. In previous studies of MAT-MI, imitating the principle of TAT, the magnetoacoustic excitation and transmission are both considered to be a point source to perform theoretical analysis and image reconstruction. However, unlike the thermal-absorption-induced 3D tissue vibration in TAT, the Lorentz-force-induced 1D tissue vibration in MAT-MI generates acoustic waves in opposite phases along the force direction to form an acoustic dipole. Considering the radiation pattern of $\cos\theta$, the dipole radiation can produce pressure attenuation with opposite phases for different transmission distances and directions. The proposed acoustic dipole radiation model of MAT-MI is verified by the experimental results of opposite vibration phases and different wave cluster amplitudes for conductivity boundaries in the collected waveforms.

In the pilot study performed by Xu and He,[11] the magnetoacoustic signals generated from a metal wire loop were collected and the reconstructed image was in good consistence with the shape of the wire loop. For the frequency at 0.5 MHz, the 0.5-mm diameter of the metal wire was much smaller than the wavelength of 3 mm. Due to the waveform superposition for the adjacent boundaries of the thin wire, only one vibration cluster could be detected and the two wire boundaries could not be differentiated. Li and Xia[14] conducted the experiment for a multi-layer cylindrical phantom with two gel columns inside and only the conductivity boundaries of the phantom with the corresponding circular and triangular cross sections were displayed in the reconstructed image, which provided an evidence for the proposed analytical forward problem solution for MAT-MI.

In the present study, the proposed theory gives a theoretical explanation of the acoustic dipole radiation for MAT-MI in acoustic diffraction transmission mode for a planar piston transducer. The numerical simulations of the collected waveform and the reconstructed image are in good agreement with the experimental results and it is proved that the reconstructed image can display only the configuration of the medium in terms of shape and size without the inner conductivity distribution visualization. The conductivity boundaries can be reconstructed with a wide striped borderline and the spatial resolution of MAT-MI can be improved with high frequency magnetic induction and a broadband transducer.[16] However, the great attenuation and nonlinear effect of thigh frequency acoustic propagation can reduce the transmission distance and lower signal-to-noise ratio (SNR) for acoustic detection. Therefore, an appropriate frequency should be selected to achieve better image effect in the experiment. In addition, the MAT-MI system is considered to be acoustically homogeneous to simplify theory deduction and numerical calculation. The acoustic reflection, refraction, and scattering are neglected. In fact, the acoustic inhomogeneity can change the

acoustic propagation direction, strengthen the acoustic scattering and lead to indeterminacy for acoustic detection, which can impair the accuracy and the determination of the image reconstruction.[26] So the magnetic distribution, the acoustic inhomogeneity and the diffraction of acoustic dipole radiation need further investigating for the inverse problem of the conductivity distribution reconstruction in MAT-MI.

5. Conclusion

In the present paper, an analytical forward problem solution of MAT-MI is proposed in explicit formula based on the acoustic dipole radiation model for a planar piston transducer. The mechanism of MAT-MI is analysed with the acoustic dipole radiation in 3D diffraction transmission mode with improved universal validity. It is demonstrated that the acoustic dipole radiation pattern produces pressure jumps at the conductivity boundaries and the corresponding vibration clusters are generated in the transducer collected waveforms. Using the back projection algorithm, the conductivity boundaries can be reconstructed with corresponding vibration intensity and phase, which are introduced by the conductivity variation. The reconstructed 2D image can display the conductivity configuration of the measured layer in terms of shape and size with obvious border stripe, while the conductivity distribution inside each medium cannot be visualized. The experimental paradigms for a two-layer cylindrical sample phantom are consistent with the numerical simulation results. Even though the conductivity reconstruction is required to be further investigated, the present studies offer a theoretical basis of conductivity imaging for MAT-MI. The favourable results also indicate that the proposed modality could be potentially used as a powerful noninvasive imaging technique to visualize the conductivity distribution with excellent spatial resolution and improved contrast.

Acknowledgment

We are grateful to He Bin (Department of Biomedical Engineering, University of Minnesota, Minneapolis 55455, USA) and Tu Juan (Institute of Acoustics, Nanjing University, Nanjing 210093, China) for their assistance in the research.

References

[1] Paulson K, Lionheart W and Pidecock M 1993 *IEEE Trans. Med. Imag.* **12** 681

[2] Zedehkoochak M, Blott B H, Hamse T K and George R F 1991 *J. Phys.* D: *Appl. Phys.* **24** 1911.

[3] Metheral P, Barber D C, Smallwood R H and Brown B H 1996 *Nature* **380** 509

[4] Al-Zeibak S, Goss D, Lyon G, Yu Z Z, Peyton A J and Beck M S 1995 *Proc. 9th Int. Conf. on Electrical Bio-Impedance* Heidelberg, Germany p. 426

[5] Griffiths H 2001 *Meas. Sci. Technol.* **12** 1126

[6] Kwon O, Woo E J, Yoon J R and Seo J K 2002 *IEEE Trans. Biomed. Eng.* **49** 160

[7] Ider Y Z and Onart S 2004 *Phys. Meas.* **25** 281

[8] Gao N and He B 2008 *IEEE Trans. Biomed. Eng.* **55** 1530

[9] Wen H 1999 *Ultrason. Imag.* **21** 186

[10] Roth B J, Basser P J and Wikswo J P 1994 *IEEE Trans. Biomed. Eng.* **41** 723

[11] Xu Y and He B 2005 *Phys. Med. Biol.* **50** 5175

[12] Li X, Xu Y and He B 2006 *J. Appl. Phys.* **99** 066112

[13] Li X, Xu Y and He B 2007 *IEEE Trans. Biomed. Eng.* **54** 323

[14] Xia R, Li X and He B 2007 *Appl. Phys. Lett.* **91** 083903

[15] Brinker K and Roth B J 2008 *IEEE Trans. Biomed. Eng.* **55** 1637

[16] Li Y L, Liu Z B, Ma Q Y and Guo X S 2010 *Chin. Phys. Lett.* **27** 084302

[17] Ma Q Y and He B 2007 *Phys. Med. Biol.* **52** 5085

[18] Ma Q Y and He B 2008 *IEEE Trans. Biomed Eng.* **55** 813

[19] Li X, Li X, Zhu S N and He B 2009 *Phys. Med. Biol.* **54** 2667

[20] Kinsler L E, Frey A R, Coppens A B and Sanders J V 2000 *Fundamentals of Acoustics* 4th edn. (New York: John Wiley & Sons)

[21] Morse P M and Feshbach H 1953 *Methods of Theoretical Physics* (New York: McGraw-Hill)

[22] Du G H, Zhu Z M and Gong X F 2001 *Fundamentals of Acoustics* (Nanjing: Nanjing University Press)

[23] Zhang H Y, Cao Y P, Sun X L, Chen X H and Yu J B 2010 *Chin. Phys.* B **19** 114301

[24] Wang L Y, Li L, Yan B, Jiang C S, Wang H Y and Bao S L 2010 *Chin. Phys.* B **19** 088106

[25] Xu Y and Wang L H 2004 *Phys. Rev. Lett.* **92** 033902

[26] Li W, Liu S B and Yang W 2010 *Chin. Phys.* B **19** 030307